Title

Bardet-Biedl Syndrome in rhesus macaques: A nonhuman primate model of retinitis pigmentosa

Authors

Peterson, Samuel M
McGill, Trevor J
Puthussery, Teresa
et al.

Publication Date

2019-12-01

DOI

10.1016/j.exer.2019.107825

Peer reviewed

HHS Public Access

Author manuscript

Exp Eye Res. Author manuscript; available in PMC 2020 December 01.

Published in final edited form as:

Exp Eye Res. 2019 December ; 189: 107825. doi:10.1016/j.exer.2019.107825.

Bardet-Biedl Syndrome in Rhesus Macaques: A Nonhuman Primate Model of Retinitis Pigmentosa

Samuel M. Peterson[1,*], **Trevor J. McGill**[2,3,*], **Teresa Puthussery**[4], **Jonathan Stoddard**[2], **Lauren Renner**[2], **Anne D. Lewis**[5], **Lois M. A. Colgin**[5], **Jacqueline Gayet**[4], **Xiaojie Wang**[2,6], **Kamm Prongay**[5], **Cassandra Cullin**[5], **Brandy Dozier**[5], **Betsy Ferguson**[1,7], **Martha Neuringer**[2,3]

[1]Division of Genetics, Oregon National Primate Research Center, Oregon Health & Sciences University, Beaverton, OR 97006, U.S.A.

[2]Division of Neurosciences, Oregon National Primate Research Center, Oregon Health & Sciences University, Beaverton, OR 97006, U.S.A.

[3]Casey Eye Institute, Oregon Health & Sciences University, Portland, OR, 97239, U.S.A.

[4]School of Optometry & Helen Wills Neuroscience Institute, University of California, Berkeley, Berkeley CA, 94720, U.S.A.

[5]Division of Comparative Medicine, Oregon National Primate Research Center, Oregon Health & Sciences University, Beaverton, OR 97006, U.S.A.

[6]Advanced Imaging Research Center, Oregon Health & Sciences University, Portland, OR, 97239, U.S.A.

[7]Department of Molecular and Medical Genetics, Oregon Health & Sciences University, Portland, OR, 97239, U.S.A.

Abstract

The development of therapies for retinal disorders is hampered by a lack of appropriate animal models. Higher nonhuman primates are the only animals with retinal structure similar to humans, including the presence of a macula and fovea. However, few nonhuman primate models of genetic retinal disease are known. We identified a lineage of rhesus macaques with a frameshift mutation

Corresponding author: Martha Neuringer, Oregon National Primate Research Center, Oregon Health & Sciences University, 505 NW 185th Ave, Beaverton, OR, 97006, neuringe@ohsu.edu.

Authors' roles

SMP, BF, MN, TJM and TP prepared the manuscript; SMP and BF conducted identification of BBS7 gene mutation and genotyping; TJM, JS, TP and JG conducted retinal histology and immunocytochemical studies; LR performed retinal imaging and electroretinography; XW analyzed MRI scans; ADL and LMAC performed necropsies and microscopic evaluation of non-ocular tissues; KP, CC and BD conducted clinical evaluations; all authors reviewed the manuscript and approved the final version.

*asterisk indicates co-first authorship

Declarations of interest: None for all authors.

Competing Interests

All authors declare that they have no competing interests.

in exon 3 of the *BBS7* gene c.160delG (p.Ala54fs) that is predicted to produce a non-functional protein. In humans, mutations in this and other *BBS* genes cause Bardet-Biedl syndrome, a ciliopathy and a syndromic form of retinitis pigmentosa generally occurring in conjunction with kidney dysfunction, polydactyly, obesity, and/or hypogonadism. Three full- or half-sibling monkeys homozygous for the *BBS7* c.160delG variant, at ages 3.5, 4 and 6 years old, displayed a combination of severe photoreceptor degeneration and progressive kidney disease. *In vivo* retinal imaging revealed features of severe macular degeneration, including absence of photoreceptor layers, degeneration of the retinal pigment epithelium, and retinal vasculature atrophy. Electroretinography in the 3.5-year-old case demonstrated loss of scotopic and photopic a-waves and markedly reduced and delayed b-waves. Histological assessments in the 4- and 6-year-old cases confirmed profound loss of photoreceptors and inner retinal neurons across the posterior retina, with dramatic thinning and disorganization of all cell layers, abundant microglia, absent or displaced RPE cells, and significant gliosis in the subretinal space. Retinal structure, including presence of photoreceptors, was preserved only in the far periphery. Ultrasound imaging of the kidneys revealed deranged architecture, and renal histopathology identified distorted contours with depressed, fibrotic foci and firmly adhered renal capsules; renal failure occurred in the 6-year-old case. Magnetic resonance imaging obtained in one case revealed abnormally low total brain volume and unilateral ventricular enlargement. The one male had abnormally small testes at 4 years of age, but polydactyly and obesity were not observed. Thus, monkeys homozygous for the *BBS7* c.160delG variant closely mirrored several key features of the human BBS syndrome. This finding represents the first identification of a naturally-occurring nonhuman primate model of BBS, and more broadly the first such model of retinitis pigmentosa and a ciliopathy with an associated genetic mutation. This important new preclinical model will provide the basis for better understanding of disease progression and for the testing of new therapeutic options, including gene and cell-based therapies, not only for BBS but also for multiple forms of photoreceptor degeneration.

Graphical Abstract

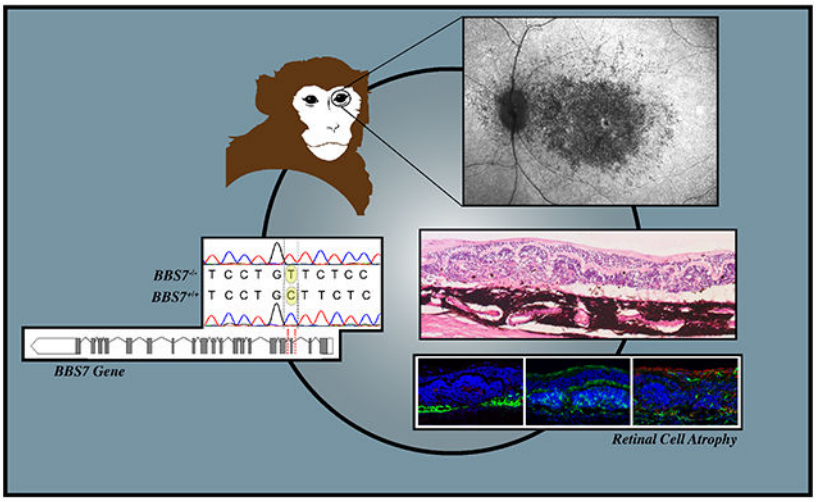

Keywords

retinitis pigmentosa; Bardet-Biedl syndrome; photoreceptor degeneration; inherited retinal degeneration; ciliopathy; blindness; nonhuman primate model

1. Introduction

The development of therapies for retinal degenerative disorders has been hampered by a lack of appropriate animal models. While transgenic rodent models are a fundamental tool, their usefulness is constrained by differences in gross retinal structure and function as well as the micro-structure of photoreceptor cells (Sahly et al., 2012). Only higher non-human primates (NHPs) have a retinal structure nearly identical to humans, including the presence of a macula and cone-rich fovea that provide the basis for high acuity central vision. Therefore, the identification or creation of NHP models is considered a critical unmet need for research into the pathogenic processes involved in inherited retinal degenerations and the preclinical testing of potential treatments (Slijkerman et al., 2015; Thompson et al., 2015; Duncan et al., 2018). However, few NHP models of genetic retinal degenerative disease have been identified. These include recent reports of retinitis pigmentosa in cynomolgus macaques of unknown genetic cause (Ikeda et al., 2018) and a rhesus macaque model of achromatopsia, a cone-specific disorder, due to a missense mutation in *PDE6C* (Moshiri et al., 2019).

The most common class of inherited retinal degenerative diseases is retinitis pigmentosa (RP), which collectively affects approximately 1:4000 people worldwide. This progressive rod-cone degeneration is caused by multiple mutations in more than 80 genes (Verbakel et al., 2019) and has autosomal recessive, autosomal dominant and X-linked forms. RP occurs in isolation or as a part of several syndromic conditions, the most prevalent being Usher syndrome and Bardet-Biedl syndrome. Bardet-Biedl syndrome (BBS) is a rare, inherited ciliopathic disorder with prevalence rates that range from 1:160,000 in European populations to 1:13,500 in individuals from Kuwait (Forsythe & Beales, 2013). It typically displays an autosomal recessive inheritance pattern and has been linked to genetic variants in 21 genes (Weihbrecht et al., 2017). Like other ciliopathic disorders, BBS can affect multiple organ systems and displays significant phenotypic variation.

Once thought to be synonymous with Laurence Moon syndrome, BBS is now considered to be genetically and phenotypically distinct (Bardet, 1995; Biedl, 1995). Clinical diagnosis of BBS is based on the appearance of at least four primary features or a combination of three primary and two secondary features (Beales et al., 1999), while definitive diagnosis can be obtained with genetic screening for known pathogenic variants. The primary features are retinal photoreceptor degeneration, obesity, polydactyly, renal anomalies, genital abnormalities and, less frequently, intellectual disabilities. Secondary features include brain abnormalities, speech disorders, eye abnormalities such as astigmatism or cataracts, brachydactyly/syndactyly, ataxia, hypertonia, diabetes mellitus, orodental abnormalities, and craniofacial dysmorphism. With the exception of polydactyly, most clinical features are absent at birth but appear and progress in severity during the first or second decade of life. BBS is phenotypically highly heterogeneous, with symptoms varying even between affected

individuals in the same family. However, photoreceptor degeneration with early macular involvement is a predominant feature and is often the first observed symptom, while kidney dysfunction becomes the main life-threatening feature. Although generally considered to be an autosomal recessive disease, heterozygous carriers of a pathogenic allele have been reported to have an increased incidence of obesity (Croft et al., 1995), renal malformations and cancer (Beale et al., 2000), and more subtle changes in retinal function, including diminished rod electroretinogram (ERG) b-wave sensitivity (Fulton et al., 2003) and local reductions in cone-mediated ERG responses within the central retina (Kim et al., 2007).

The molecular basis for BBS resides in impaired ciliogenesis or the dysfunction of immotile (primary) cilia (Ansley et al., 2003; Weihbrecht et al., 2017; Zaghloul et al., 2009). Unlike motile cilia, which are found only in specific tissues like the lining of the trachea, inner ear or fallopian tubes, primary cilia are found on most eukaryotic cells and function in chemical sensation and signal transduction rather than the generation of flow or movement. Structurally, primary cilia are similar to motile cilia in that they are comprised of an axoneme formed from 9 pairs of microtubule doublets projecting from a basal body, but lack the cytoskeletal motor protein dynein and the additional central microtubule pair required to generate movement. The BBSome protein complex, a vital component of the basal body, is central to sorting and vesicular trafficking of membrane proteins to or within cilia (Davis et al., 2007; Jin et al., 2010). Retinal degeneration in BBS is believed to be linked to structural and functional deficits in the connecting cilium between the photoreceptor inner and outer segments, which is critical for the continuous regeneration of outer segment disk membranes (Mockel et al., 2011; Bujakowska et al., 2017). BBS proteins play an essential role in the intraflagellar transport which traffics proteins and membrane components through the connecting cilium, and disruption of the BBSome can result in mislocalization of inner and outer segment proteins (Datta et al., 2015; Weihbrecht et al., 2017). All 21 identified BBS genes are involved in cilia function, either as a structural member of the BBSome complex (*BBS1, BBS2, BBS4, BBS5, BBS7, BBS8, BBS9, BBS17* and *BBS18*), the chaperonin complex, which is required for BBSome formation (*BBS6, BBS10 and BBS12*), basal body (*BBS13, BBS14, BBS15 and BBS16*) or other related processes (*BBS3, BBS11, BBS19, BBS20 and NPHP1*). *BBS7*, a key component of the BBSome, is unique from other BBSome complex members in that it directly interacts with the chaperonin complex. Discovered through its sequence similarity to *BBS1 and BBS2, BBS7* was further linked to BBS through genetic screening of BBS pedigrees (Badano et al., 2003). At least 31 pathogenic variants have been identified in *BBS7*, which account for ~2% of all BBS cases (Khan et al., 2016).

Caenorhabditis elegans with *BBS7* mutations show ciliary structural deficits and mislocalization of proteins involved in intraflagellar transport (Blacque et al., 2004). Transgenic rodent and morphant fish models with targeted disruption of *BBS* genes partially recapitulate human BBS phenotypes and are an important resource for studying pathogenic processes and for initial screening of potential therapeutic options (Mei et al., 2014; Yen et al., 2006; Zhang et al., 2013). However, as noted above, for the translation of results to human patients, there is a need for a NHP model with a much higher degree of homology to humans in retinal structure. In this report, we describe the discovery of a spontaneous NHP BBS model which helps to address this need. Three related rhesus macaques housed at the

Oregon National Primate Research Center (ONPRC) presented with retinal dystrophy and renal anomalies that were linked to a frameshift mutation in the *BBS7* gene. To our knowledge, this is the first reported, genetically confirmed case of BBS-associated disease in NHPs, and more generally, the first NHP model of retinitis pigmentosa due to a known genetic mutation.

2. Materials and Methods

2.1 Animals

All animal care and procedures were approved by the OHSU Institutional Animal Care and Use Committee and were in compliance with the National Institutes of Health Guide for the Care and Use of Laboratory Animals, 8th Edition (National Research Council, 2011), the ARVO Statement for the Use of Animals in Ophthalmic and Vision Research, and the ARRIVE guidelines (Kilkenny et al., 2010). All animal research was conducted at the ONPRC at Oregon Health & Science University, which is accredited by the Association for Assessment and Accreditation of Laboratory Animal Care, International.

Three related rhesus macaques *(Macaca mulatta)* with retinal degeneration and kidney pathology were identified. All were born and raised at ONPRC and were housed in the same large social group until the emergence of clinical signs required removal to single or paired caging for veterinary observation and evaluation. Retinal degeneration in the first case (Case 1, 4-year old male) was identified postmortem. In the second case (Case 2, 6-year-old female), retinal imaging was conducted just prior to euthanasia for kidney failure. In these two animals, retinas were examined by histology and immunohistochemistry, and kidneys and other organs were evaluated for pathology. A third living case (Case 3, female, 3.5-years old at the time of identification and initial assessment) underwent retinal imaging, evaluation of retinal function by full-field electroretinography (ERG), magnetic resonance brain imaging, and evaluation of kidney status by ultrasound, blood biochemistry and urinalysis. For reference, the age ratio between humans and macaques is considered to be 1:3, so the 3.5 - 6 year age range is roughly equivalent to 14 - 18 human years.

The demographics, evaluations conducted, and phenotypic information for each case are briefly summarized in Table 1. In addition, clinical and histopathological records were examined for abnormalities in heterozygotes. Retinal imaging, renal ultrasound, and histopathology of the retina, kidney and other organs were obtained in one 25-year-old heterozygote, and retinal imaging in a 16-year old heterozygote. Genetic sequencing information from 464 additional rhesus macaques was used to define the causative gene and construct a pedigree. Clinical parameters, retinal imaging, electroretinography and brain imaging from representative unaffected rhesus macaques provided normative data for comparison to the affected cases, as detailed in the relevant sections.

2.2 Clinical evaluation

Physical exams and diagnostics were performed by clinical veterinarians at ONPRC. Abdominal ultrasounds were performed using an Esaote MyLab Delta or MyLab5 system (Fishers, IN). Noninvasive blood pressure was measured on Case 3 while sedated with

ketamine (10mg/kg, IM) and in lateral recumbency; three consecutive measures were collected using a PetMap machine (Tampa, FL) with an appropriately sized cuff placed around the biceps. Complete blood count, serum chemistry panel, urinalysis and culture were performed by the ONPRC Clinical Pathology Laboratory.

2.3 Genetic sequencing and pedigree analysis

DNA was extracted from buffy coat samples with a Maxwell 16 Blood DNA Purification Kit. Whole genome sequencing was performed at Medgenome (Foster City, CA). Sequence reads (150 bp paired-end) were aligned to the macaque genome (Mmul_8.0.1) with BWA-MEM (Li, 2013). Genetic variants were called with the Genome Analysis Toolkit following best practices (McKenna et al., 2010). Variants were evaluated using the Macaque Genotype and Phenotype Resource (mGAP): https://mgap.ohsu.edu (Bimber et al., 2019), which includes population level genotype data for a total of ~30 million variants discovered in 341 rhesus macaques at the ONPRC or in other National Primate Research Center rhesus macaque breeding colonies. The candidate *BBS7* variant was PCR amplified using primers (BBS7ex3F – ATGCCAAAGGTGCCTTACAA; BBS7ex3R – GGCATTTCTGACCATAATCCA). Amplicons were treated with exonuclease I and shrimp alkaline phosphatase (New England Biolabs, Inc.) and sequenced on an ABI 3730XL DNA Analyzer (LifeTech, Inc.) at the ONPRC Molecular Biology Core. Sequence traces were analyzed using A Plasmid Editor software. Further genotyping for pedigree analysis was performed using a custom designed TaqMan assay (ThermoFisher Scientific, Inc.).

2.4 In vivo retinal imaging

Multimodal retinal imaging was conducted on Cases 2 and 3 and compared with existing normative data from age-matched unaffected animals. For this procedure, anesthesia was induced by an intramuscular injection (IM) of Telazol (1:1 mixture of tiletamine hydrochloride and zolazepam hydrochloride, 3.5-5mg/kg) and maintained with ketamine (1-2mg/kg, IM) as required. Supplemental oxygen was provided as needed via nasal cannula at 0.5-1.0L/min, and heart rate and peripheral blood oxygen saturation were monitored by pulse oximetry. Rectal temperature was maintained between 37.0°C and 38.0° C by water-circulating heated pads placed underneath the animal. Subjects were positioned prone with the head supported by a chinrest. Prior to image acquisition, the pupils were dilated to a minimum of 8 mm using phenylephrine (2.5%) and tropicamide (1%) eyedrops. Specula were used to keep the eyelids open, and clear plano contact lenses were inserted and centered over the cornea.

Color fundus photographs were acquired using a digital Cannon EOS 6D camera connected to a Zeiss FF450 fundus camera system. Multiple color fundus images spanning the posterior retina were collected for each eye. A Heidelberg Spectralis spectral domain-optical coherence tomography (SD-OCT) system with a standard 30° lens was used to acquire the following cross-sectional images of the retina: a standard scan (30°x 25° automatic real-time tracking setting (ART):20; 61 lines with ~120 μm spacing), plus two high density scans (#1:15°x 10° ART:20; 49 lines with ~60 μm spacing; and #2: 15°x 5° ART:20; 97 lines with ~30 μm spacing) for characterization of the macula/fovea and salient features of interest. Spectralis segmentation software (EyeExplorerVersion 6.12.1) was used to segment retinal

layers, with manual inspection and correction of each slice. The Spectralis Blue Peak mode was then used to acquire quantitative fundus autofluorescence (qFAF) images from both eyes. Prior to acquiring qFAF images, the retina was visualized and brought into focus using the infrared imaging mode. The system was then switched to its short-wavelength excitation laser (488 nm), and final focus adjustments were made to optimize the visualization of the retina. The fundus was first bleached with a minimum 30-second exposure to the blue laser to minimize contribution from photoreceptors to the FAF signal (Delori et al., 2011; McGill et al., 2016). Images were collected using the non-normalized acquisition setting with manual sensitivity set to 90 for each image to allow quantitative measurements. The signal/noise ratio was enhanced by averaging 100 scans. In the 3.5-year-old animal, retinal fluorescein angiography was performed using an ultra-widefield retinal imaging camera (Optos California). After proper positioning of the pupil for optimal imaging of the fundus, sodium fluorescein (~6 mg/kg IV) was injected into the saphenous vein and followed immediately by a series of photographs documenting the state of the retinal vessels and retinal pigment epithelium. Following completion of imaging, contacts and speculums were removed and erythromycin ointment was applied to each eye.

2.5 Electroretinography

Retinal function of Case 3 and unaffected controls was assessed with full-field electroretinography (ERG) using an Espion Diagnosys system (Lowell, MA). Anesthesia was induced with a combination of ketamine (10 mg/kg IM), xylazine (1 mg/kg IM) and glycopyrrolate (0.01mg/kg IM) and maintained with additional quarter to full doses of each agent as necessary. Pupils were dilated with tropicamide plus phenylephrine eyedrops. Supplemental oxygen was provided via nasal cannula at 0.5-1.0L/min, rectal temperature was maintained between 37.0°C and 38.0°C by water-circulating heated pads, and el ectrocardiogram, respiration rate, peripheral blood oxygen saturation and body temperature were monitored throughout the procedure. A custom bipolar contact lens electrode (Hansen Ophthalmic Development Lab, Coralville, IA) was placed on the cornea, and corneal lubrication was maintained with hypromellose eyedrops. The monkey was positioned in front of a ganzfeld diffusing sphere. Rod-dominated responses were recorded after 30 minutes of dark adaptation to an ascending series of short-wavelength flashes at intensities from threshold to rod b-wave saturation (0.001 to 50 cd-s/m^2), averaging 2 to 5 responses at each intensity. Cone-dominated responses were isolated using 1) long-wavelength flashes at 2 Hz superimposed on a photopic adapting background (80 cd-s/m^2) at intensities from 0.1 – 10 cd-s/m^2), averaging 5 responses at each intensity; and 2) white flashes flickering at 31 Hz, averaging 15 responses at each intensity.

2.6 Magnetic resonance brain imaging

In vivo brain MRI scans were acquired from Case 3 at 4 years of age, and from 18 normal age-matched controls (4.0±0.25 years of age), using a 3T Siemens Prisma system with a 16-channel pediatric head coil as the radiofrequency receiver. Anesthesia was induced with ketamine (15 g/kg IM) followed by intubation and maintenance with inhaled 1-1.5% isoflurane in 100% oxygen. A 3D magnetization-prepared rapid acquisition gradient echo (MP-RAGE) sequence was used to acquire T_1-weighted (T_1W) volumes with pulse sequence parameters TR/TI/TE (repetition time/inversion time/echo time) of 2600/913/3.4 ms and flip

angle of 8°. A 3D fast spin-echo sequence (SPACE) was used to acquire T_2-weighted (T_2W) volumes with TR/TE = 3200/385 ms and echo train length of 183. Both T_1W and T_2W volumes were acquired at 0.5 mm isotropic resolution and 3 repetitions were acquired for each pulse sequence.

The three volumes per each sequence collected were averaged together after motion correction and B_1 field inhomogeneity correction. The motion correction was achieved by rigid-body registration using the "FLIRT" function of the FSL software suite (https://fsl.fmrib.ox.ac.uk/fsl/fslwiki). The B_1 field inhomogeneity was corrected using a B-spline approximation routine and a hierarchical optimization scheme implemented by "N4BiasFieldCorrection" in Advanced Normalization Tools (Tustison et al., 2010). The resulting T_1W volume was skull-stripped using the FSL "BET" function and then rigid-body aligned to an adult rhesus macaque T_1W template (INIA19, Rohlfing et al., 2012) using "FLIRT", giving a transformed T_1W volume in the INIA19 space. The averaged T_2W volume was rigid-body registered to the T_1W volume. As a result, the transformed T_1W and T_2W volume of monkey 3 and the INIA19 T_1W template were all in the same coordinate space, facilitating subsequent qualitative and quantitative comparison.

2.7 Retinal immunohistochemistry

Eyes were collected from Cases 1 and 2 and from a 25-year-old *BBS7* heterozygote within 10 minutes of euthanasia and fixed in 4% paraformaldehyde for at least 24 hours. They were then hemisected, embedded in optimum cutting temperature compound, frozen, and serially sectioned at 14 μm. Sections through the optic nerve and fovea were thawed and stained for hematoxylin and eosin to evaluate gross morphological changes. Adjacent slides used for immunofluorescence staining were thawed and dried and then incubated for 30-60 minutes in a phosphate-buffered saline-based blocking buffer containing 4-10% horse serum, 0.5-1.0% Triton-X 100, with or without 1.0% bovine serum albumin, and with or without 0.025% NaN_3. Sections were then incubated in primary antibodies diluted in blocking buffer overnight at either 4°C or 25°C. Antibodies used included PKCα to label rod bipolar cells, RPE65 to label retinal pigmented epithelial (RPE) cells, IBA1 to label retinal microglial cells, GFAP to label reactive Müller glial cells, and cone arrestin (Albini et al., 2004; Li et al., 2003; Zhang et al., 2001) to label cones (See Table 2 for details). The following morning, sections were rinsed repeatedly and then incubated with species-appropriate AlexaFluor secondary antibodies at a concentration of 1:300-1:800 for one hour at room temperature. Nuclear layers were counterstained with 4′,6-diamidino-2-phenylindole, dihydrochloride (DAPI) or with Hoechst 33342. Images were captured on Zeiss confocal micros5copes with 20x objectives.

2.8 Postmortem Examinations

Cases 1 and 2 and 11 heterozygotes were euthanized using standard methods for euthanasia of nonhuman primates consistent with the recommendations of the American Veterinary Medical Association's Panel on Euthanasia (June 2013). Full diagnostic necropsies were performed immediately following euthanasia by board certified veterinary pathologists. All major organs were evaluated grossly and representative tissues were collected for

microscopic examination. Tissues were fixed in 10% neutral buffered formalin, embedded in paraffin, sectioned at 5 μm and stained with hematoxylin and eosin.

3. Results

3.1 Clinical Evaluation

Case 1, a 4-year-old male, had a clinical history which included low body weight for age (3.7 kg; normal range 5-7 kg) and multiple episodes of diarrhea that temporarily resolved with treatment. Such cases of chronic colitis are a common and well-documented clinical issue in rhesus macaques (Laing et al., 2018; Westreich et al., 2019; Kapusinszky et al., 2017). During one representative episode, blood chemistry and complete blood counts showed elevated blood urea nitrogen (BUN) of 68 mg/dL (normal range 10-27) and serum phosphorus (10.8 mg/dL; normal range 4.1-7.8) and leukocytosis (white blood cell count 16.6 x 10^9/L; normal range 4.2-13.6), which were considered secondary to diarrhea, dehydration and infection. The animal was treated for this condition multiple times with the antibiotic azithromycin, in combination with bismuth subsalicylate, simethicone, oral electrolytes, psyllium and/or probiotics. “Stargazing” behavior (staring upward) was noted in group housing; the animal’s behavior was otherwise unremarkable and it was able to maintain normal social relationships in its natal group. Cage-side behavioral observations in an unfamiliar environment noted inaccurate targeting of treats and inability to properly locate perches and toys. After repeated episodes of diarrhea, euthanasia was elected due to persistent health issues, stunted growth and failure to respond to treatment.

Case 2, a 6-year-old female, was initially evaluated for abdominal distension and poor stool quality. Body weight was normal at 6.6 kg. Cage-side observations of behavior, including purposeful but inaccurate movement towards food treats, suggested visual deficits; the animal’s behavior appeared otherwise normal. Significant clinical pathology findings included leukocytosis (white blood cell count 18.6 x 10^9/L) and azotemia (elevated BUN of 55 mg/dL). Urine was hyposthenuric (specific gravity 1.005), alkaline (pH 8), and contained a moderate number of erythrocytes and leukocytes. Abdominal ultrasound revealed deranged renal architecture, with pitted cortical surfaces, indistinct renal margins, multiple well-defined hypoechoic wedges, and rhomboid-shaped cortical regions bilaterally (Fig. 1). Following a preliminary diagnosis of renal azotemia, short-term intravenous saline diuresis was followed by oral replacement therapy, but azotemia persisted despite normal food and fluid consumption. Therefore, euthanasia was elected due to diagnosis of renal failure.

Case 3, female, had no abnormal clinical history prior to identification of homozygosity for the *BBS7* c.160delG variant by genotype analysis at 3.5 years of age. Visual deficits were noted when she was removed from the social group to a novel environment for clinical evaluation; no other behavioral deficits were observed. Physical exam revealed mild obesity (7.3 kg body weight), subjectively small uterus, and firm left kidney. By abdominal ultrasound, both kidneys had diffusely increased echogenicity (left more affected), a nonspecific indicator of renal disease, with well-demarcated capsular surfaces. Urinalysis results were essentially normal, with hyposthenuria (specific gravity 1.002), neutral pH (7.0), trace blood, and negative bacterial culture, and no azotemia was present on serum chemistry panel. Average non-invasive blood pressure values were 140 mmHg systolic, 60

mmHg diastolic, and 90 mmHg mean arterial pressure and were confirmed on repeat exam. These values indicate hypertension, a possible sequela of renal disease. This case is under continuing evaluation.

3.2 Genetic screening

Genetic analysis began following the identification of two full-sibling cases. Although whole genome sequence on either case was not initially available, we leveraged the mGAP database of sequence variants identified in 293 ONPRC rhesus macaques, including primary relatives of the two cases, to identify candidate variants. All sequence variants were filtered for 1) predicted impact on protein translation/function using SnpEff classification of High or Moderate functional impact (Cingolani et al., 2012) or with a CADD score > 20.0 (Kircher et al., 2014), 2) population-level allele frequency < 0.1; 3) presence of the allele among first degree relatives of the affected monkeys; and 4) relevance of the variant-linked gene and gene-associated diseases. These filters identified a single basepair deletion in exon 3 of *BBS7*: c.160delG (p.Ala54fs) as a strong candidate variant based on the function of the *BBS7* gene and the predicted damaging impact of the resulting translational frame shift and premature termination (Fig. 2). The mGAP database, which did not include any affected monkeys at the time of analysis, did not identify any c.160delG homozygous genotypes, but did reveal a full sibling to an affected subject to be a heterozygote. While the c.160delG variant doesn't specifically match any reported human variants, the predicted effect on rhesus BBS7 translation is similar to the seven human *BBS7* frameshift or premature termination variants reported in ClinVar. All seven of the human frame shift variants are classified as pathogenic or likely pathogenic and associated with Bardet-Biedl Syndrome (Landrum et al., 2016). Two other variants also passed the variant filters, a missense variant in Cyclin Dependent Kinase 16 (CDK16: c.1448G>A (p.Arg483Gln)) and an early termination in Glutamyl Aminopeptidase (ENPEP: c.1150C>T (p.Gln384*)). While neither variant could be formally excluded, their gene functions make them less likely to contribute to the observed macaque disease phenotype (Nanus et al., 1990; Tang et al., 2006).

Subsequent whole genome sequencing of the initial affected monkey confirmed it to be homozygous for the *BBS7* c.160delG (p.Ala54fs) variant. Sanger re-sequencing of both affected cases also confirmed them each to be homozygous for the *BBS7* allele, while the sire and dam of affected siblings were heterozygous. A genotyping screen of the extended macaque pedigree using a custom-design TaqMan assay confirmed an autosomal recessive inheritance pattern, identifying 61 carriers (39 living) and one additional homozygous individual (Case 3). No unaffected homozygotes were identified in the most current mGAP database update (V.1.8), which includes genotype data for 348 ONPRC macaques ($p < 0.0001$; Fisher's exact test). Based on the significant association of the *BBS7* c.160delG variant, and the similar clinical features of the rhesus macaque cases and Bardet Biedl Syndrome, we herein refer to the three genotyped, affected cases as $BBS7^{-/-}$.

3.3 Retinal imaging

Color fundus imaging revealed distinct retinal atrophy in the macula and surrounding the optic nerve, as illustrated in Fig. 3 for Case 2 and in Fig. 4 for Case 3. Vessels of both superior and inferior retinal arcades were significantly thinner than in the eyes of age-

matched controls, and there was significant loss of retinal vasculature in the macula. Fundus autofluorescence (FAF) imaging showed intense, diffuse hyperfluorescence across the posterior pole combined with distinct macular hypoautofluorescence indicative of RPE cell loss. FAF and fluorescein angiography imaging also confirmed a significant loss of retinal vasculature in the macula. OCT imaging through the optic nerve and fovea illustrated a severe thinning of the retina with loss of distinct retinal layers. No comparable pathology has been observed in our normative database of retinal imaging in over 1000 rhesus monkeys.

3.4 Electroretinography

In Case 3, the full-field ERG under scotopic conditions showed absence of the a-wave and severe amplitude reduction and slowing of the b-wave (Fig. 4I) compared to unaffected controls (Fig. 4H). The photopic ERG similarly showed near-abolishment of the a-wave, which was detectable only at the highest intensity, and minimal b-waves (Fig. 4J, K). The waveform for the flicker ERG was virtually undetectable even at the brightest intensity (Fig. 4L, M).

3.5 Magnetic resonance brain imaging

Axial (upper) and sagittal (lower) T_1W and T_2W images for Case 3 at 4 years of age are shown in Fig. 5A together with T_1W images for a representative age-matched unaffected monkey. The location of the image planes is indicated by the white dashed lines on the red brain schematics at the left. Reduced brain size is evident in the scans. Fig. 5B illustrates that the total brain volume of Case 3 at 4 years of age was below the normal range, based on comparison with values for 18 age-matched controls (4.0 ± 0.25 years) that had MRI scans acquired and processed by identical methods in the ONPRC MRI facility (data from Shnitko et al., 2019). Specifically, the volume of 74.1 ml was 30% below the control mean, or approximately 3 standard deviations (S.D. = 10.1) below the control mean of 105.6 ml; this value is therefore beyond the 99.7% confidence limit, translating to a 99.7% probability of differing from normal values. Registration-based segmentation of 10 brain regions (cortex, white matter, brainstem, cerebellum, thalamus, caudate, globus pallidus, putamen, hippocampus, amygdala) showed that their fractional volumes, when compared to values from the reference INIA19 atlas, were proportional to the reduction in total brain volume; that is, no region showed a selective reduction.

In addition, both T_1W and T_2W images of Case 3 demonstrated a dilated posterior horn of the right lateral ventricle (Fig. 5A). Large foci extending as far posterior as the occipital pole (hypo-intense on the T_1W image and hyper-intense on the T_2W image) are evident on the axial and sagittal images; such ventricle dilation is not normally seen and is absent in the representative control.

3.6 Retinal histology and immunofluorescence

Histological analysis of Case 1 (4 years) and Case 2 (6 years) documented profound loss of photoreceptors and disturbance of the organization of the inner retina across the posterior pole (Figs. 3D–F and 6), confirming *in vivo* imaging results for Case 2 (Fig. 3A–C). The central retina of both animals was markedly thinned and disorganized with disruption of

normal retinal lamination. To further assess retinal changes, we used immunohistochemistry to examine the RPE (RPE65 antibody staining), cones (cone arrestin), microglia (IBA1), rod bipolar cells (PKCα) and the extent of reactive gliosis (GFAP) in the central, mid-peripheral and far peripheral regions of the retina (Fig. 6). For comparison, images also are shown for a 25-year-old male heterozygote with normal retinal structure. Overall, in both cases degeneration was more marked in central retina compared to peripheral retina, and disease progression was more advanced in the older subject. RPE cells (Fig 6A, RPE65) showed loss of normal structure in central retina with proliferation, migration and dropout, whereas apparently normal RPE structure was retained in far peripheral retina, particularly in the younger animal. The outer nuclear layer was nearly completely degenerated in the central retina of both animals, while some residual cones (cone arrestin positive cells) and rods (cone arrestin negative cells) remained in the mid-peripheral and far peripheral outer retina in both animals. These residual photoreceptors showed aberrant morphology with truncated inner and outer segments. In mid-peripheral retina, cones represented the majority of residual cell bodies in the ONL, suggesting a rod-cone sequence of degeneration. There were abundant microglia (Fig. 6B, IBA1), particularly in the central retina of the older animal, whereas GFAP immunoreactivity (Fig. 6B, GFAP) was more marked in the peripheral retina. In both animals, rod bipolar cells (Fig. 6C, PKCα) showed aberrant morphology and lamination in central retina, with loss of normal dendritic and axonal organization. In contrast, rod bipolar cells in far peripheral retina appeared relatively normal in both animals. Taken together, these findings provide support for a progressive photoreceptor degeneration and accompanying glial changes advancing from central to peripheral retina.

3.7 Pathology of the kidneys

In Case 1 (4 years), the capsules of both kidneys were moderately adherent. The right kidney had multiple cortical depressions, and both kidneys had several wedge-shaped areas of pallor within the cortex (Fig. 7D). The renal microscopic findings included interstitial fibrosis with a mononuclear inflammatory infiltrate, and multiple dilated renal tubules with lining epithelium that was often hyperplastic (Fig. 7E,F).

Grossly, the kidneys of Case 2 (6 years) resembled Case 1, but the lesions were more advanced. At necropsy, gross examination showed severe renal scarring and parenchymal loss. The kidney contours were extensively distorted by depressed, fibrotic foci, and the renal capsules were firmly adhered. On sectioned surface, there was severe cortical loss with streaks and wedge-shaped foci of fibrosis that extended to and often traversed the medulla (Fig. 7G). A medullary cyst was present in the left kidney. The pelvises were irregular and contracted; while both kidneys were severely affected, the right one was affected more. Microscopic examination showed severe nephron loss with replacement fibrosis, tubule atrophy, ectasia, occasional neutrophilic casts and interstitial inflammatory infiltrates composed of lymphocytes and plasma cells with few macrophages and rare eosinophils (Fig. 7H). Cystic tubules were lined by either attenuated epithelium or proliferative epithelium occasionally forming micropapillary projections (Fig. 7I). Glomeruli were often sclerotic and rarely cystic.

3.8 Pathology of other tissues

Other findings in Case 1 included a proliferative, chronic-active typhlocolitis and mesenteric lymphoid hyperplasia, consistent with the animal's clinical history of chronic colitis. No significant microscopic findings were noted in the brain; brain weight was 82.9 g, at the low end of the normal range (mean ± S.D. = 96.1 ± 8.7 g for rhesus males, n=219; Herndon et al., 1998). The testes were small for age, weighing 0.73 g and 0.79 g; these weights are closer to the average testicular weight of 2-year-old rhesus macaques (0.59 g) than 4-year-olds (14.52 g), and histologic evaluation confirmed an immature state. Micropenis was not observed.

In Case 2, additional pathologic findings included proliferative, chronic-active proliferative typhlocolitis and secondary reactive amyloidosis affecting the jejunum, ileum, splenic white pulp and inguinal lymph nodes. Brain was unremarkable both grossly and microscopically, with a weight of 75.5 g, again at the low end of the normal range (mean ± S.D. = 86.1 ± 8.0 g for rhesus females, n=180; Herndon et al., 1998). The ovaries were of normal weight and histologically appeared normal, containing numerous follicles in various stages of development as well as post-ovulatory follicles.

3.9 Findings in BBS7$^{+/-}$ heterozygotes

As illustrated in Fig. 6, the retinas of a heterozygote examined by immunohistochemistry showed normal structure even at the advanced age of 25 years. Brain weights of 6 male and 6 female heterozygotes, obtained from necropsy records, were normal (Table 1). The 25-year-old animal also had a 1.2 cm cyst on the right cranial kidney, an occasional finding especially in older animals. Pathology evaluation of 10 additional carriers showed no gross lesions or other evidence of renal disease; in one case, microscopic evaluation showed amyloidosis secondary to chronic colitis. Two carriers had suspected or documented cardiac arrhythmias but no cardiac defects; one of these was obese and had clitoral hypertrophy. Blood chemistry values of 37 living carriers showed none with elevated BUN or creatinine; the one exception was a case of dehydration secondary to severe colitis, with values normalizing after fluid therapy. Thus, no consistent retinal, brain or renal pathologies were observed in heterozygotes.

Heterozygotes had normal fertility. The sire of the 3 cases had 83 offspring, and two other carrier males in group housing had 110 and 45 offspring. The dam of the first 2 cases had 9 infants in 9 years, the maximum possible given that rhesus monkeys have one infant per annual breeding season. A sampling of 7 carrier females of reproductive age in group housing showed an average rate of production of 0.8 infants per year, compared to the maximum rate of 1 per year, indicating normal fertility.

4. Discussion

BBS is a rare ciliopathic disorder for which there is currently no treatment. The phenotype observed in rhesus monkeys with a c.160delG variant in the *BBS7* gene parallels key features of human BBS, including both photoreceptor dystrophy with severe macular degeneration and kidney pathology leading to kidney failure.

The animals evaluated in this study showed a very advanced stage of retinal degeneration as adolescents or young adults. The extensive retinal disorganization across all retinal layers in the central retina exceeded that typically observed in humans with BBS or other forms of retinitis pigmentosa. However, the phenotype of this disease is highly variable, and due to the rare occurrence of BBS7, few human reports are available for comparison. Furthermore, atrophy and disorganization of all retinal layers is a characteristic observed in a number of animal models of retinal degeneration. In particular, retinal remodeling (phase 3 remodelling as defined in Marc et al., 2003) is observed in several models after the near total loss of photoreceptors, and includes neuronal and glial cell remodeling and vascular and cellular invasions of the retina.

The existence of hypogonadism, a common feature in human BBS, cannot be conclusively determined in the macaque model at this point. In the one 4-year-old male subject (Case 1), testes were smaller and more immature than generally observed at this age; however, given wide variation in pubertal development between individual 4-year-old male macaques, the significance of the decreased testicular size is uncertain. Polydactyly, another common aspect of the human disease, was not seen in these three cases. Obesity was not consistently observed, but interpretation of body weights is complicated by other factors. Case 3 was mildly obese; however, Case 1 had chronic gastrointestinal illness that limited weight gain, and Case 2 had kidney disease. Therefore, no conclusion currently can be drawn about the propensity for obesity in animals with the c.160delG variant.

Brain abnormalities in MRI scans have been reported in a small number of BBS patients, with highly variable presentations including reduced gray matter volume (Baker et al., 2011; Braun et al., 2014), reduced white matter volume (Keppler-Noreuil et al., 2011), mild cortical and/or cerebellar atrophy or frontal cortical dysplasia (Rooryck et al., 2007), and/or increased ventricular volume (Baker et al., 2011; Keppler-Noreuil et al., 2011 Rooryck et al., 2007). In the one BBS7$^{-/-}$ monkey available for brain MRI scans, total brain volume was reduced 30% below the normal mean and the right lateral ventricle was enlarged. Brain weights of the other two cases, measured at necropsy, were in the lower quartile of the normal range. These data suggest a possible effect of the *BBS7* c.160delG variant on brain growth that will require confirmation in future cases. Other than deficits clearly attributable to poor vision, no obvious behavioral deficits were seen in these cases. Remarkably, their social behavior in a stable social group, and in a familiar environment, appeared normal to experienced observers. The one unusual behavior that was noted in one case was “stargazing”, a tendency to look upward.

It is important to note the limitations of this initial report of BBS in monkeys: the present study was constrained to the examination of three affected macaques, and only after they had undergone substantial retinal disease progression. Considering the wide phenotypic variability observed in human cases of BBS, it is possible that additional symptoms will manifest in future cases. A more comprehensive description of the syndrome will require the propagation of additional affected animals that can be followed longitudinally from birth and throughout the course of the disease, including its early, subclinical stages. To this end, targeted breeding of BBS7 carriers is now underway.

While we are confident in the pathogenicity of the identified variant, it will be important to continue genetic screening efforts, especially of individuals in the affected pedigree, to confirm this conclusion. Furthermore, we can use the identification of additional carriers to construct targeting breeding groups to propagate this model and, conversely, avoid inclusion of carriers in the general rhesus breeding colony.

As sequencing technologies improve and genome sequencing efforts expand, it is likely that more naturally occurring disease models will be discovered in macaques and other nonhuman primates. The ease with which the observed phenotype in this study was connected to a pathogenic allele can be directly attributed to the exceptional resource of the publicly-available Macaque Genotype and Phenotype (mGAP) database (https://mgap.ohsu.edu), which substantially facilitated both the search for candidate variants and the exclusion of commonly observed variants (Bimber et al, 2019). It is vital that this and other similar resources be maintained and expanded to facilitate the discovery of other valuable NHP models of a range of human diseases.

Small animal models are vital to studies of disease mechanisms and the investigation of novel therapeutics. However, the results of such studies do not always translate accurately to human patients. NHP models are ideal for bridging this gap due to their increased genetic and physiological homology to humans. With respect to eye diseases, only monkeys and apes closely match the key structural features of the human retina, including its macula and fovea, as well as multiple aspects of visual function including high acuity and color vision. Furthermore, rodents lack calyceal processes, the rigid microvilli that surround the inner segment-outer segment connecting cilium in primate photoreceptors (Sahly et al., 2012), limiting their usefulness for studies of retinal ciliopathies such as Usher syndrome and BBS. Therefore, macaques with the BBS7 syndrome will provide a uniquely valuable and optimal translational model for understanding disease pathogenesis from its earliest stages, and for preclinical testing of gene and cell therapies. Furthermore, the importance and usefulness of the model extends well beyond this specific disease. As a form of retinitis pigmentosa, a family of photoreceptor degenerations which together are the most prevalent cause of inherited retinal degeneration, the BBS7 syndrome can serve as a desperately-needed model for this entire class of inherited retinal degenerative diseases. In addition, as this is, to our knowledge, the first genetic, naturally-occurring nonhuman primate model of a ciliopathy, it can provide a model to better understand this class of retinopathies that also includes Usher syndrome, the most prevalent cause of deaf-blindness. Thus, the identification of this syndrome provides the potential for the first highly translatable preclinical model for the study of pathogenic mechanisms of photoreceptor degeneration and the testing of therapeutic options.

5. Conclusions

We have identified a naturally-occurring rhesus monkey model of Bardet-Biedl syndrome, a syndromic form of retinitis pigmentosa, caused by a frameshift variant in the *BBS7* gene. By 4-6 years of age, affected individuals show a severe photoreceptor degeneration that is most severe in the macula, as well as kidney disease progressing to renal failure. Propagation of this model will provide the first nonhuman primate model of retinitis pigmentosa with a

known genetic cause, which will be invaluable for preclinical testing of gene, cell-based, and other therapies for this family of blinding disorders.

Acknowledgements

The authors thank David J. Wilson, MD and Mark Pennesi, MD, PhD for consultation on the clinical presentation of Bardet-Biedl syndrome, the staff of the ONPRC Department of Comparative Medicine for valuable technical assistance and support, and Akshay Pulavarty for technical assistance in retinal immunohistochemistry.

Funding

This work was supported by the National Institutes of Health (grant R24OD021324 to BF, R21EY031106 to MN, P51OD011092 and S10RR024585 to ONPRC, P30EY010572 to Casey Eye Institute, R01EY024265 to TP and P30EY003176 to UC Berkeley Vision Science Core) and by Research to Prevent Blindness (Stein Innovation Award to MN, Sybil B. Harrington Special Scholar Award to TJM, and unrestricted grant to Casey Eye Institute). The funding sources had no involvement in study design, the collection, analysis and interpretation of data, or the writing of the report.

Abbreviations

ART	automatic real-time tracking
BBS	Bardet-Biedl syndrome
BUN	Blood urea nitrogen
DAPI	4′,6-diamidino-2-phenylindole, dihydrochloride
ERG	electroretinogram
GFAP	glial fibrillary acidic protein
H&E	hematoxylin and eosin
IBA1	ionized calcium binding adaptor molecule 1
mGAP	Macaque Genotype and Phenotype Resource
MRI	magnetic resonance imaging
NHP	non-human primates
OCT	optical coherence tomography
ONPRC	Oregon National Primate Research Center
PKC-α	protein kinase C alpha
RPE	retinal pigmented epithelium
qFAF	quantitative fundus autofluorescence
SD-OCT	spectral-domain optical coherence tomography

References

Albini T, Rao N, Li A, Craft CM, Fuji GY, DeJuan E 2004 Limited macular translocation: clinicopathologic case report. Ophthalmology, 111(6), 1209–1214. doi: 10.1016/j.ophtha.2003.10.021 [PubMed: 15177973]

Ansley SJ, Badano JL, Blacque OE, Hill J, Hoskins BE, Leitch CC, Kim JC, Ross AJ, Eichers ER, Teslovich TM, Mah AK, Johnsen RC, Cavender JC, Lewis RA, Leroux MR, Beales PL, Katsanis N (2003). Basal body dysfunction is a likely cause of pleiotropic Bardet-Biedl syndrome. Nature, 425(6958), 628–633. doi: 10.1038/nature02030 [PubMed: 14520415]

Badano JL, Ansley SJ, Leitch CC, Lewis RA, Lupski JR, & Katsanis N (2003). Identification of a novel Bardet-Biedl syndrome protein, BBS7, that shares structural features with BBS1 and BBS2. Am J Hum Genet, 72(3), 650–658. doi: 10.1086/368204 [PubMed: 12567324]

Baker K, Northam GB, Chong WK, Banks T, Beales P, and Baldeweg T (2011). Neocortical and hippocampal volume loss in a human ciliopathy: A quantitative MRI study in Bardet-Biedl syndrome. Am J Med Genet A, 155A, 1–8. doi: 10.1002/ajmg.a.33773 [PubMed: 21204204]

Bardet G (1995). On congenital obesity syndrome with polydactyly and retinitis pigmentosa (a contribution to the study of clinical forms of hypophyseal obesity). 1920. Obes Res, 3(4), 387–399. [PubMed: 8521156]

Beales PL, Reid HA, Griffiths MH, Maher ER, Flinter FA, Woolf AS (2000). Renal cancer and malformations in relatives of patients with Bardet-Biedl syndrome. Nephrol Dial Transplant, 15(12), 1977–85. [PubMed: 11096143]

Beales PL, Elcioglu N, Woolf AS, Parker D, & Flinter FA (1999). New criteria for improved diagnosis of Bardet-Biedl syndrome: results of a population survey. J Med Genet, 36(6), 437–446. [PubMed: 10874630]

Biedl A (1995). A pair of siblings with adiposo-genital dystrophy. 1922. Obes Res, 3(4), 404. [PubMed: 8521158]

Bimber BN, Yan MY, Peterson SM, Ferguson B (2019). mGAP: the macaque genotype and phenotype resource, a framework for accessing and interpreting macaque variant data, and identifying new models of human disease. BMC Genomics, 20(1), 176. doi: 10.1186/s12864-019-5559-7 [PubMed: 30841849]

Blacque OE, Reardon MJ, Li C, McCarthy J, Mahjoub MR, Ansley SJ, Badano JL, Mah AK, Beales PL, Davidson WS, Johnsen RC, Audeh M, Plasterk RH, Baillie DL, Katsanis N, Quarmby LM, Wicks SR, Leroux MR (2004). Loss of *C. elegans* BBS-7 and BBS-8 protein function results in cilia defects and compromised intraflagellar transport. Genes Dev, 18(13), 1630–42. doi:10.1101/gad.1194004 [PubMed: 15231740]

Braun J-J, Noblet V, Durand M, Scheidecker S, Zinetti-Bertschy A, Foucher J, Marion V, Muller J, Riehm S, Dollfus H, Kremer S (2014). Olfaction evaluation and correlation with brain atrophy in Bardet-Biedl syndrome. Clin Genet, 86, 521–529. doi: 10.1111/cge.12391 [PubMed: 24684473]

Bujakowska K, Liu Q, Pierce EA (2017). Photoreceptor cilia and retinal ciliopathies. Cold Spring Harb Perspect Biol, 9(10):a028274. doi:10.1101/cshperspect.a028274 [PubMed: 28289063]

Cingolani P, Platts A, Wang LL, Coon M, Nguyen T, Wang L, Land SJ, Lu X, Ruden DM (2012). A program for annotating and predicting the effects of single nucleotide polymorphisms, SnpEff: SNPs in the genome of Drosophila melanogaster strain w1118; iso-2; iso-3. Fly (Austin), 6(2):80–92. doi: 10.4161/fly.19695. [PubMed: 22728672]

Croft JB, Morrell D, Chase CL, Swift J (1995). Obesity in heterozygous carriers of the gene for Bardet-Biedl syndrome. Am J Med Gen, 55(1), 12–15. doi: 10.1002/aimg.1320550105

Davis RE, Swiderski RE, Rahmouni K, Nishimura DY, Mullins RF, Agassandian K, Philp AR, Searby CC, Andrews MP, Thompson S, Berry CJ, Thedens DR, Yang B, Weiss RM, Cassell MD, Stone EM, Sheffield VC (2007). A knockin mouse model of the Bardet-Biedl syndrome 1 M390R mutation has cilia defects, ventriculomegaly, retinopathy, and obesity. Proc Natl Acad Sci USA, 104(49), 19422–19427. doi: 10.1073/pnas.0708571104 [PubMed: 18032602]

Datta P, Allamargot C, Hudson JS, Andersen EK, Bhattarai S, Drack AV, Sheffield VC, Seo S (2015). Accumulation of non-outer segment proteins in the outer segment underlies photoreceptor

degeneration in Bardet-Biedl syndrome. Proc Natl Acad Sci USA, 112(32), E4400–4409. doi:10.1073/pnas.1510111112 [PubMed: 26216965]

Delori F, Greenberg JP, Woods RL, Fischer J, Duncker T, Sparrow J, & Smith RT (2011). Quantitative measurements of autofluorescence with the scanning laser ophthalmoscope. Invest Ophthalmol Vis Sci, 52(13), 9379–9390. doi:10.1167/iovs.11-8319 [PubMed: 22016060]

Duncan JL, Pierce EA, Laster AM, Daiger SP, Birch DG, Ash JD, Iannaccone A, Flannery JG, Sahel JA, Zack DJ, Zarbin MA; and the Foundation Fighting Blindness Scientific Advisory Board. (2018). Inherited retinal degenerations: current landscape and knowledge gaps. Transl Vis Sci Technol, 7(4):6. doi: 10.1167/tvst.7.4.6.

Forsythe E, Beales PL (2013). Bardet-Biedl syndrome. Eur J Hum Genet, 21(1), 8–13. doi:10.1038/ejhg.2012.115 [PubMed: 22713813]

Fulton AB, Hansen RM, Glynn RJ (1993). Natural course of visual functions in the Bardet-Biedl syndrome. Arch Ophthalmol, 111:1500–1506. [PubMed: 8240105]

Herndon JG, Tigges J, Klumpp SA, Anderson DC (1998). Brain weight does not decrease with age in adult rhesus monkeys. Neurobiol Aging, 19(3):267–272. [PubMed: 9662002]

Ikeda Y, Nishiguchi KM, Miya F, Shimozawa N, Funatsu J, Nakatake S, Fujiwara K, Tachibana T, Murakami Y, Hisatomi T, Yoshida S, Yasutomi Y, Tsunoda T, Nakazawa T, Ishibashi T, Sonoda KH (2018). Discovery of a cynomolgus monkey family with retinitis pigmentosa. Invest Ophthalmol Vis Sci, 59(2), 826–830. doi: 10.1167/iovs.17-22958 [PubMed: 29411010]

Jin H, White SR, Shida T, Schulz S, Aguiar M, Gygi SP, Bazan JF, Nachury MV (2010). The conserved Bardet-Biedl syndrome proteins assemble a coat that traffics membrane proteins to cilia. Cell, 141(7): 1208–1219. doi: 10.1016/j.cell.2010.05.015 [PubMed: 20603001]

Kapusinszky B, Ardeshir A, Mulvaney U, Deng X, Delwart E (2017). Case-control comparison of enteric viromes in captive rhesus macaques with acute or idiopathic chronic diarrhea. J Virol, 91(18). pii: e00952–17. doi: 10.1128/JVI.00952-17 [PubMed: 28659484]

Keppler-Noreuil KM, Blumhorst C, Sapp JC, Brinckman D, Johnston J, Nopoulos PC, Biesecker LG (2011). Brain tissue- and region-specific abnormalities on volumetric MRI scans in 21 patients with Bardet-Biedl syndrome (BBS). BMC Med Genet, 12, 101. doi: 10.1186/1471-2350-12-101. [PubMed: 21794117]

Khan SA, Muhammad N, Khan MA, Kamal A, Rehman ZU, & Khan S (2016). Genetics of human Bardet-Biedl syndrome, an update. Clin Genet, 90(1), 3–15. doi:10.1111/cge.12737 [PubMed: 26762677]

Kilkenny C, Browne WJ, Cuthill IC, Emerson M, Altman DG (2010). Improving Bioscience Research Reporting: The ARRIVE Guidelines for Reporting Animal Research. PLoS Biol, 8(6): e1000412. doi:10.1371/journal.pbio.1000412 [PubMed: 20613859]

Kim LS, Fishman GA, Seiple WH, Szlyk JP, & Stone EM (2007). Retinal dysfunction in carriers of Bardet-Biedl syndrome. Ophthalmic Genet, 28(3), 163–168. doi :10.1080/13816810701537440 [PubMed: 17896315]

Kircher M, Witten DM, Jain P, O'Roak BJ, Cooper GM, Shendure J (2014). A general framework for estimating the relative pathogenicity of human genetic variants. Nat Genet, 46(3), 310–315. doi: 10.1038/ng.2892 [PubMed: 24487276]

Laing ST, Merriam D, Shock BC, Mills S, Spinner A, Reader R, Hartigan-O'Connor DJ (2018). Idiopathic colitis in rhesus macaques Is associated With dysbiosis, abundant enterochromaffin cells and altered T-cell cytokine expression. Vet Pathol, 55(5), 741–752. doi: 10.1177/0300985818780449 [PubMed: 29929446]

Landrum MJ, Lee JM, Benson M, Brown G, Chao C, Chitipiralla S, et al. (2016). ClinVar: public archive of interpretations of clinically relevant variants. Nucleic Acids Res, 44, D862–D868. doi: 10.1093/nar/gkv1222 [PubMed: 26582918]

Li A, Zhu X, Brown B, Craft CM. (2003). Gene expression networks underlying retinoic acid-induced differentiation of human retinoblastoma cells. Invest Ophthalmol Vis Sci, 44(3), 996–1007. doi:10.1167/iovs.02-0434 [PubMed: 12601020]

Li H (2013). Aligning sequence reads, clone sequences and assembly contigs with BWA-MEM. arXiv preprint arXiv:1303.3997.

Marc RE, Jones BW, Watt CB, Strettoi E (2003). Neural remodeling in retinal degeneration. Prog Retin Eye Res, 22, 607–655. doi:10.1016/S1350-9462(03)00039-9 [PubMed: 12892644]

McGill TJ, Renner LM, & Neuringer M (2016). Elevated fundus autofluorescence in monkeys deficient in lutein, zeaxanthin, and omega-3 fatty acids. Invest Ophthalmol Vis Sci, 57(3), 1361–1369. doi:10.1167/iovs.15-18596 [PubMed: 27002296]

McKenna A, Hanna M, Banks E, Sivachenko A, Cibulskis K, Kernytsky A, Garimella K, Altshuler D, Gabriel S, Daly M, DePristo MA (2010). The Genome Analysis Toolkit: a MapReduce framework for analyzing next-generation DNA sequencing data. Genome Res, 20(9), 1297–1303. doi:10.1101/gr.107524.110 [PubMed: 20644199]

Mei X, Westfall TA, Zhang Q, Sheffield VC, Bassuk AG, & Slusarski DC (2014). Functional characterization of Prickle2 and BBS7 identify overlapping phenotypes yet distinct mechanisms. Dev Biol, 392(2), 245–255. doi:10.1016/j.ydbio.2014.05.020 [PubMed: 24938409]

Mockel A, Perdomo Y, Stutzmann F, Letsch J, Marion V, Dollfus H (2011). Retinal dystrophy in Bardet-Biedl syndrome and related syndromic ciliopathies. Prog Retin Eye Res, 30(4), 258–274. doi:10.1016/j.preteyeres.2011.03.001 [PubMed: 21477661]

Moshiri A, Chen R, Kim S, Harris RA, Li Y, Raveendran M, Davis S, Liang Q, Pomerantz O, Wang J, Garzel L, Cameron A, Yiu G, Stout JT, Huang Y, Murphy CJ, Roberts J, Gopalakrishna KN, Boyd K, Artemyev NO, Rogers J, Thomasy SM (2019) A nonhuman primate model of inherited retinal disease. J Clin Invest. 129(2), 863–874. doi: 10.1172/JCI123980. [PubMed: 30667376]

Nanus DM, Pfeffer LM, Bander NH, Bahri S, Albino AP (1990). Antiproliferative and antitumor effects of alpha-interferon in renal cell carcinomas: correlation with the expression of a kidney-associated differentiation glycoprotein. Cancer Res, 50, 4190–4194. [PubMed: 2364374]

National Research Council (2011). Guide for the Care and Use of Laboratory Animals: Eighth Edition Washington, DC: The National Academies Press 10.17226/12910.

Rooryck C, Pelras S, Chateil JF, Cances C, Arveiler B, Verloes A, Lacombe D, Goizet C (2007). Bardet-Biedl syndrome and brain abnormalities. Neuropediatrics, 38(1), 5–9. doi: 10.1055/s-2007-981466 [PubMed: 17607597]

Sahly I, Dufour E, Schietroma C, Michel V, Bahloul A, Perfettini I, Pepermans E, Estivalet A, Carette D, Aghaie A, Ebermann I, Lelli A, Iribarne M, Hardelin JP, Weil D, Sahel JA, El-Amraoui A, Petit C (2012). Localization of Usher 1 proteins to the photoreceptor calyceal processes, which are absent from mice. J Cell Biol. 199(2), 381–399. doi: 10.1083/jcb.201202012 [PubMed: 23045546]

Shnitko T, Liu Z, Wang X, Grant KA, Kroenke CD (2019). Chronic alcohol drinking slows brain development in adolescent and young adult nonhuman primates. eNeuro, 6(2), eNeuro.0044-19.2019. doi: 10.1523/ENEURO.0044-19.2019

Slijkerman RWN, Song F, Astuti GDN, Huynen MA,. Wijk E, Stieger K, Collin RWJ. (2015). The pros and cons of vertebrate animal models for functional and therapeutic research on inherited retinal dystrophies. Prog Ret Eye Res, 48:137–159. doi.org/10.1016/j.preteyeres.2015.04.004

Tang X, Guilherme A, Chakladar A, Powelka AM, Konda S, Virbasius JV, Nicoloro SMC, Straubhaar J, Czech MP (2006). An RNA interference-based screen identifies MAP4K4/NIK as a negative regulator of PPAR-gamma, adipogenesis, and insulin-responsive hexose transport. Proc Nat Acad Sci, 103, 2087–2092. doi: 10.1073/pnas.0507660103 [PubMed: 16461467]

Thompson DA, Ali RR, Banin E, Branham KE, Flannery JG, Gamm DM, Hauswirth WW, Heckenlively JR, Iannaccone A, Jayasundera KT, Khan NW, Molday RS, Pennesi ME, Reh TA, Weleber RG, Zacks DN; Monaciano Consortium (2015). Advancing therapeutic strategies for inherited retinal degeneration: Recommendations from the Monaciano Symposium. Invest Ophthalmol Vis Sci, 56(2), 918–931. doi: 10.1167/iovs.14-16049 [PubMed: 25667399]

Tustison NJ, Avants BB, Cook PA, Zheng Y, Egan A, Yushkevich PA, Gee JC (2010). N4ITK: improved N3 bias correction. IEEE Trans Med Imag, 29, 1310–1320. doi: 10.1109/TMI.2010.2046908

Verbakel SK, van Huet RAC, Boon CJF, den Hollander AI, Collin RWJ, Klaver CCW, Hoyng CB, Roepman R, Klevering BJ (2018). Non-syndromic retinitis pigmentosa. Prog Retin Eye Res, 66:157–186. doi: 10.1016/j.preteyeres.2018.03.005. [PubMed: 29597005]

Weihbrecht K, Goar WA, Pak T, Garrison JE, DeLuca AP, Stone EM, Scheetz TD , Sheffield VC (2017). Keeping an eye on Bardet-Biedl syndrome: a comprehensive review of the role of Bardet-Biedl syndrome genes in the eye. Med Res Arch, 5(9). doi: 10.18103/mra.v5i9.1526

Westreich ST, Ardeshir A, Alkan Z, Kable ME, Korf I, Lemay DG (2019). Fecal metatranscriptomics of macaques with idiopathic chronic diarrhea reveals altered mucin degradation and fucose utilization. Microbiome, 7(1), 41. doi: 10.1186/s40168-019-0664-z [PubMed: 30885266]

Yen HJ, Tayeh MK, Mullins RF, Stone EM, Sheffield VC, Slusarski DC (2006). Bardet-Biedl syndrome genes are important in retrograde intracellular trafficking and Kupffer's vesicle cilia function. Hum Mol Genet, 15(5), 667–677. doi:10.1093/hmg/ddi468 [PubMed: 16399798]

Zaghloul NA, Katsanis N (2009). Mechanistic insights into Bardet-Biedl syndrome, a model ciliopathy. J Clin Invest, 119(3), 428–437. doi:10.1172/JCI37041. [PubMed: 19252258]

Zhang Q, Nishimura D, Vogel T, Shao J, Swiderski R, Yin T, Searby C, Carter CS, Kim GH, Bugge K, Stone EM, Sheffield VC (2013). *BBS7* is required for BBSome formation and its absence in mice results in Bardet-Biedl syndrome phenotypes and selective abnormalities in membrane protein trafficking. J Cell Sci, 126(Pt 11), 2372–2380. doi :10.1242/jcs.111740 [PubMed: 23572516]

Zhang Y, Li A, Zhu X, Wong CH, Brown B, Craft CM (2001). Cone arrestin expression and induction in retinoblastoma cells In Retinal Degeneration Diseases and Experimental Therapy, Kluwer Academic, Plenum Publishers, N.Y., 309–318. 10.1007/978-1-4615-1355-1_33

Highlights

- A rhesus monkey family was identified with Bardet-Biedl syndrome (BBS)
- Affected monkeys show key features of BBS including retina and kidney degeneration
- The syndrome is linked to a frameshift mutation in *BBS7*, part of the BBSome
- This is the first monkey model of retinitis pigmentosa with known genetic cause
- This model will have great value for testing new therapies for blinding diseases.

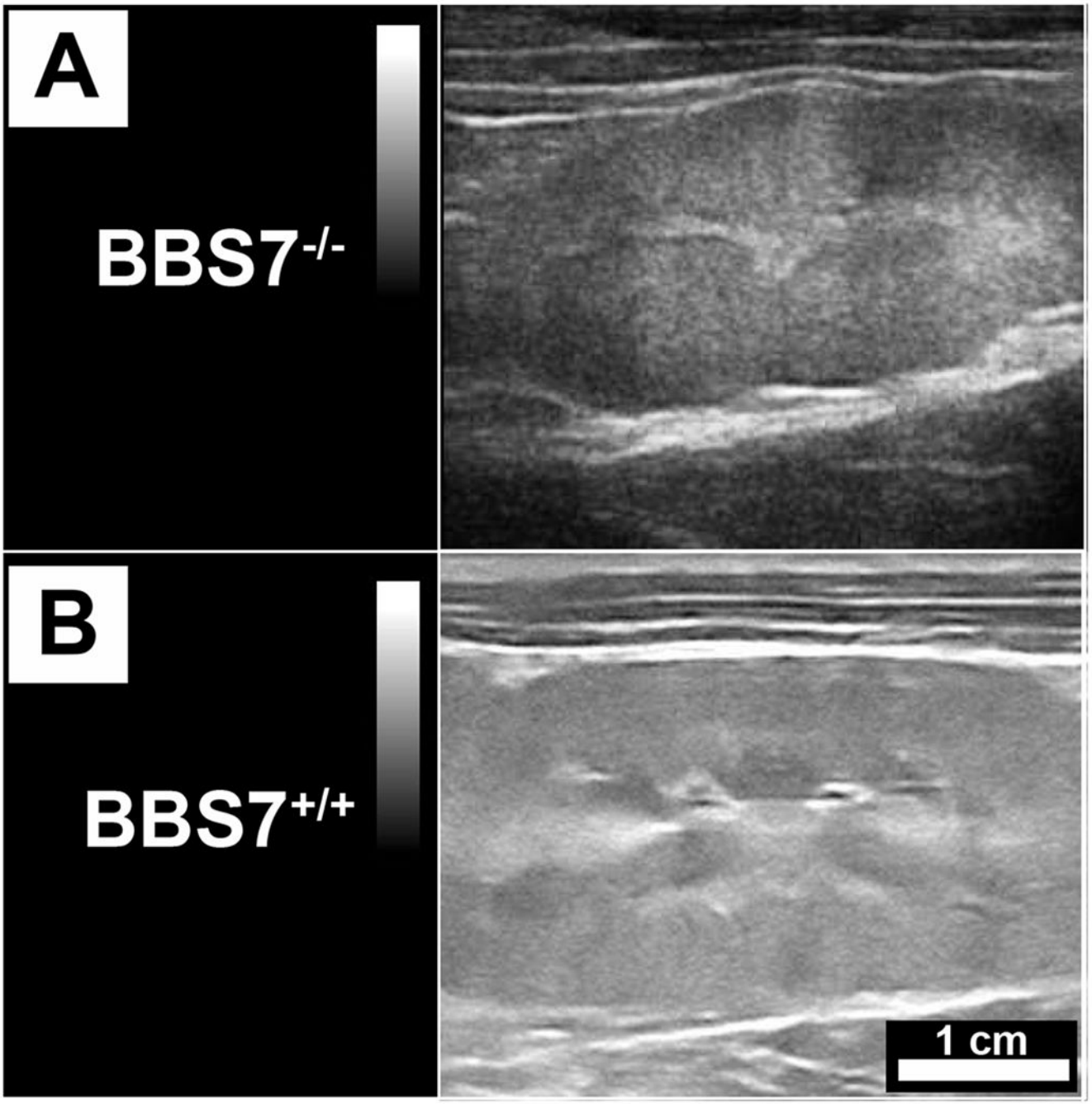

Fig. 1.

Abnormal renal morphology in Case 2, a 6-year-old macaque with the *BBS7*$^{-/-}$ mutation. Sagittal abdominal ultrasound images of the affected macaque (A) reveal kidneys with bilateral hypoechoic lesions, pitted cortical surfaces and indistinct margins, features not found in normal controls (representative example in B). The scale bar applies to both A and B.

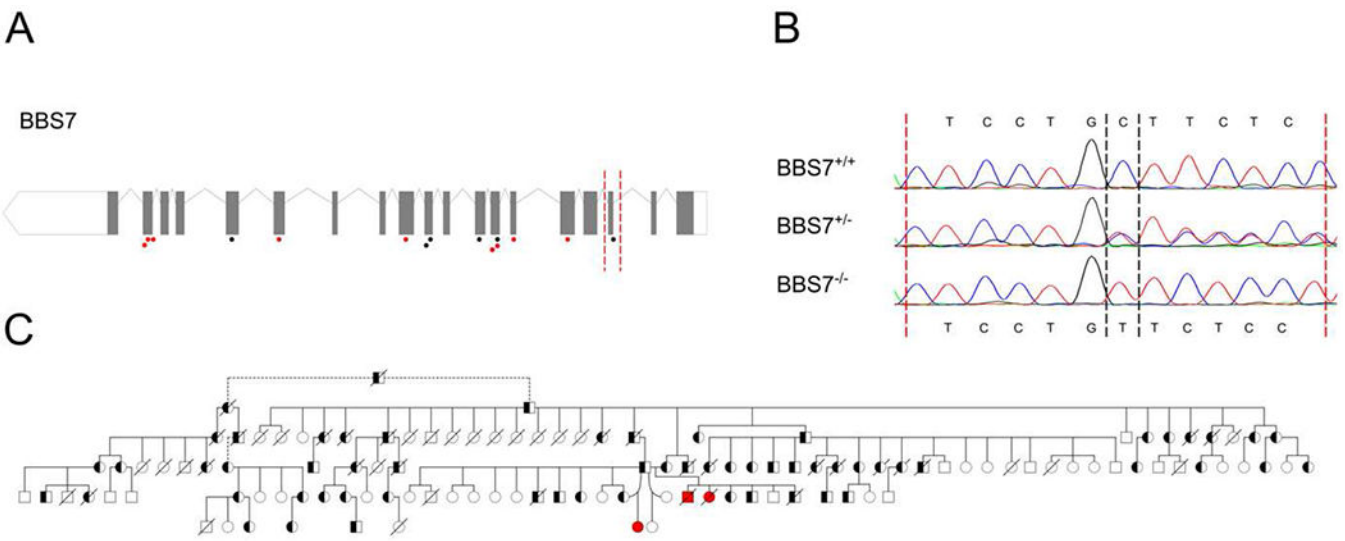

Fig. 2.

Identification of frameshift deletion in *BBS7* of rhesus macaques. A) The *BBS7* gene has 19 exons and encodes a 715 amino acid protein. A frameshift deletion (c. 160delG) was discovered in exon 3 (dashed red lines). Dots below exons indicate approximate locations of pathogenic frameshift and early termination (red dots) or missense (black dots) mutations in humans with BBS. B) Sanger sequence chromatograms identified homozygous affected monkeys and heterozygous parents. First affected nucleotide is highlighted with dashed black lines. C) Expanded pedigree analysis supports autosomal recessive inheritance. Males are indicated by squares and females by circles. *BBS7*$^{-/-}$ affected individuals are indicated with solid fill, while genotyped carriers have partial shading. Unconfirmed parentage is marked with a dashed line. Slashes indicate deceased individuals; note that these include animals ascertained over 3 decades for which death was due to age-related, natural or experimental causes.

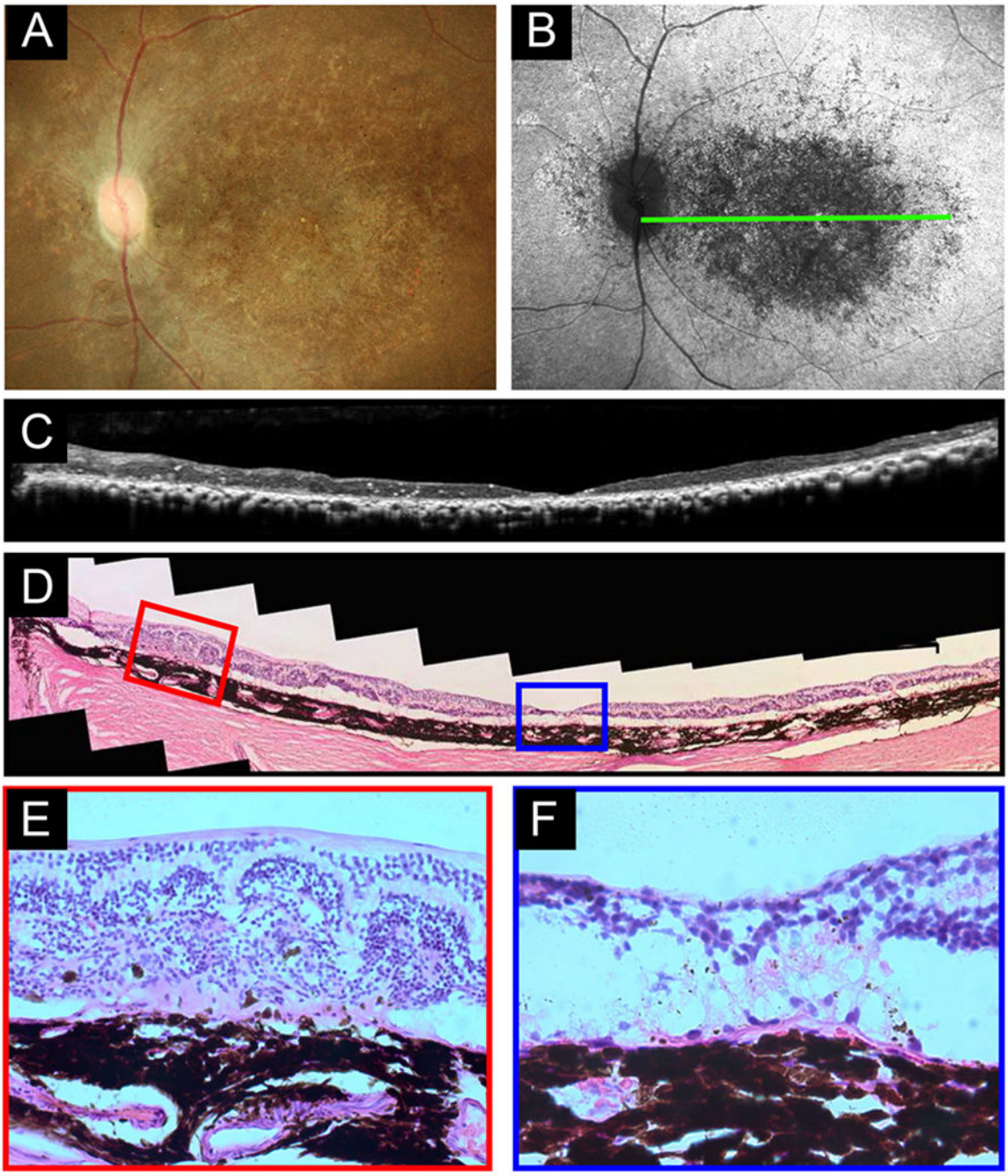

Fig. 3.

In vivo and histological imaging of Case 2, a 6-year-old rhesus macaque with the *BBS7*$^{-/-}$ mutation. A) Color fundus photography revealed significant retinal atrophy in the macula and fovea with a lack of obvious retinal vasculature throughout the posterior pole. B) Fundus autofluorescence confirmed the lack or reduction in retinal vasculature, but also showed intense, diffuse hyperfluorescence across the posterior pole in contrast with distinct macular hypoautofluorescence indicative of pigmented epithelial cell atrophy. C) Optical coherence tomography (OCT) identified severe atrophy of all retinal layers. D) Hematoxylin and eosin

staining of a section of retina (D, E and F) closely matched to the OCT section revealed severe atrophy of retinal cells in all layers, rosettes of inner retinal and glial cells (E, red outline in D) and a complete loss of outer retinal cells in the fovea (F, blue outline in D).

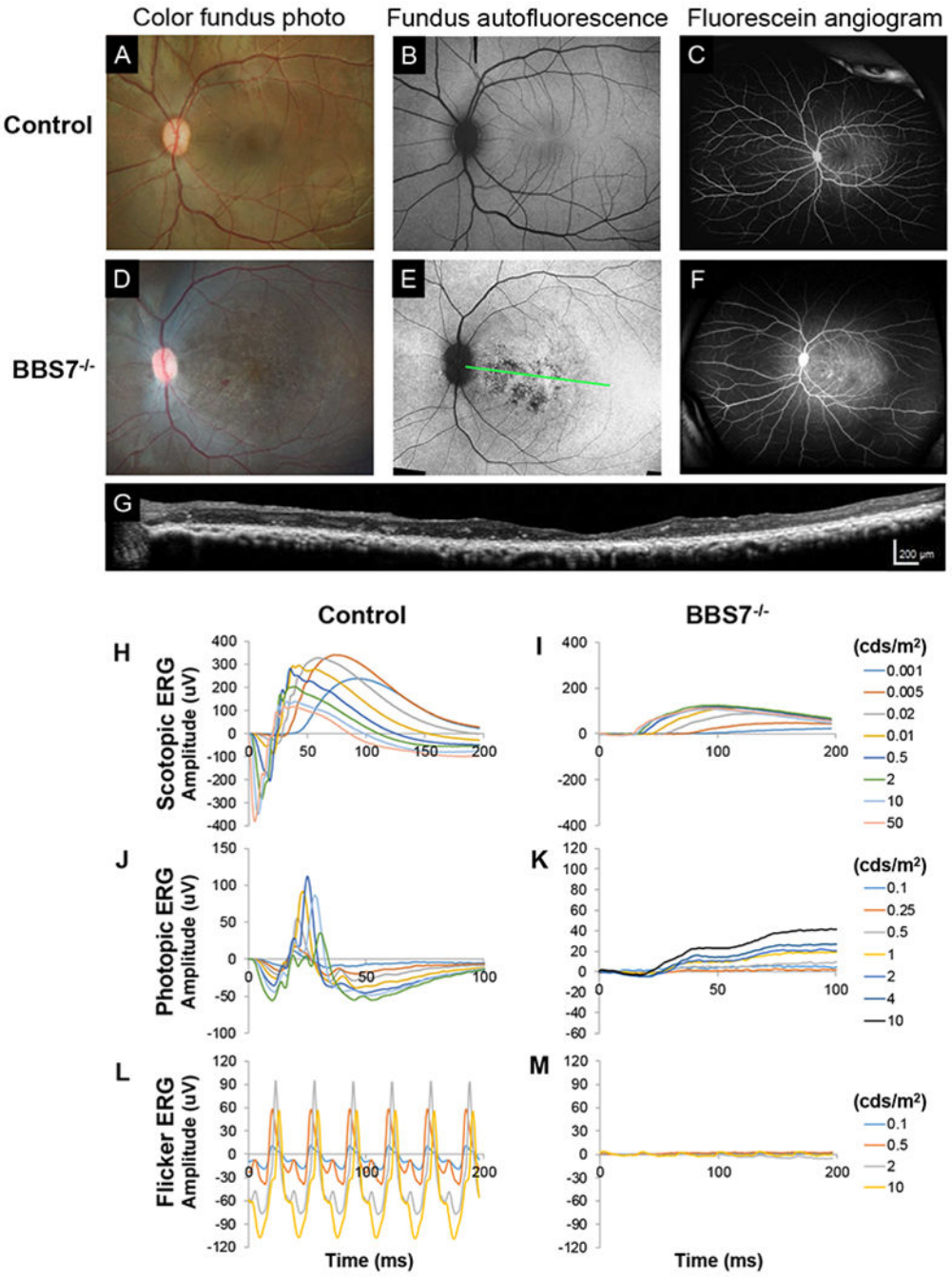

Fig. 4.

Retinal imaging and functional assessment of *BBS7*$^{-/-}$ Case 3 at 3.5 years of age (D, E, F, I, K, M) in comparison with an age-matched unaffected monkey (A, B, C, H, J, L). D) color fundus photo of the *BBS7*$^{-/-}$ case shows abnormal pigmentation and vasculature. E) FAF imaging shows widespread hyperfluorescence but patchy macular hypofluorescence consistent with RPE atrophy. F) Ultra-wide-field fluorescein angiography shows absence of normal macular RPE screening of choroidal fluorescence and localized transmission defects. G) OCT scan, corresponding to the green line in E, illustrates severe thinning and loss of

retinal layers. The lower panels illustrate severely reduced amplitudes and delayed time courses of both the scotopic (I), photopic (K) and flicker (M) ERG in comparison to a representative unaffected monkey (H, J, L).

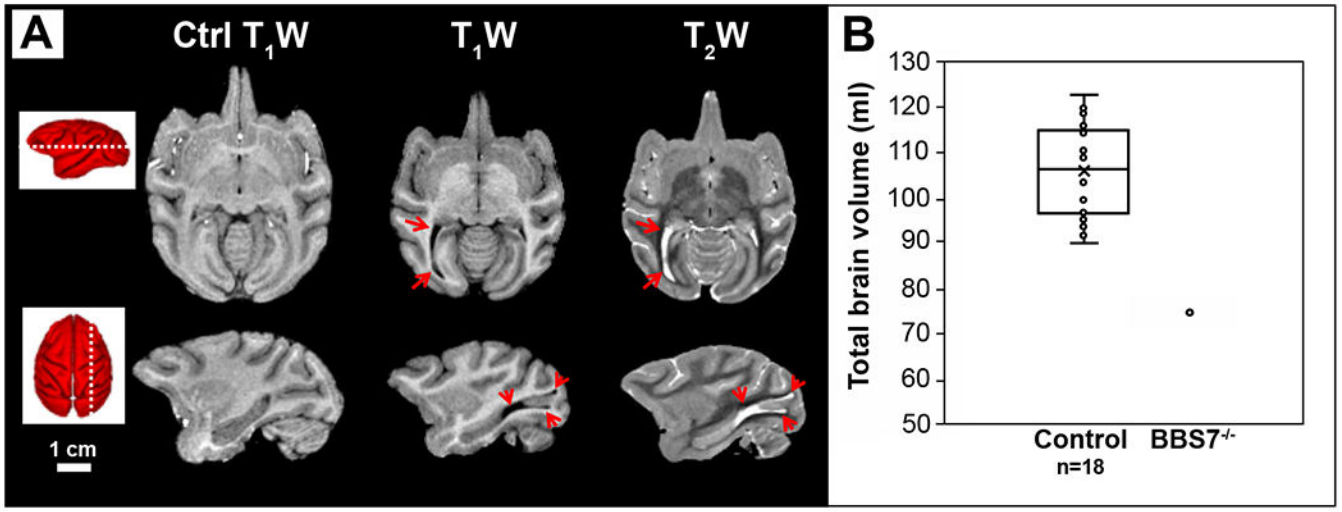

Fig. 5.

Brain MRI findings in *BBS7*$^{-/-}$ Case 3 at 4 years of age. A) Axial (top) and sagittal (bottom) images are shown for T_1-weighted (T_1W) images from a representative age-matched control (left), and for T_1W (middle) and T_2-weighted (T_2W, right) images of Case 3. Levels of the images are indicated by the dashed white lines on the red 3D brain surface schematic. The brain of Case 3 appears notably smaller than the age-matched unaffected control, and a dilated posterior horn of the right lateral ventricle is indicated by hypo-intense and hyper-intense foci (red arrows) on T_1W and T_2W images, respectively. B) Total brain volume for Case 3 is shown compared with 18 age-matched unaffected monkeys (4.0 ± 0.25 years). In the box-and-whisker plot of the control data, open dots = individual values, box = interquartile range, middle line = median, x = mean, and whiskers = range. Total brain volume for Case 3 is reduced by 30%, or over 3 standard deviations, below the control mean.

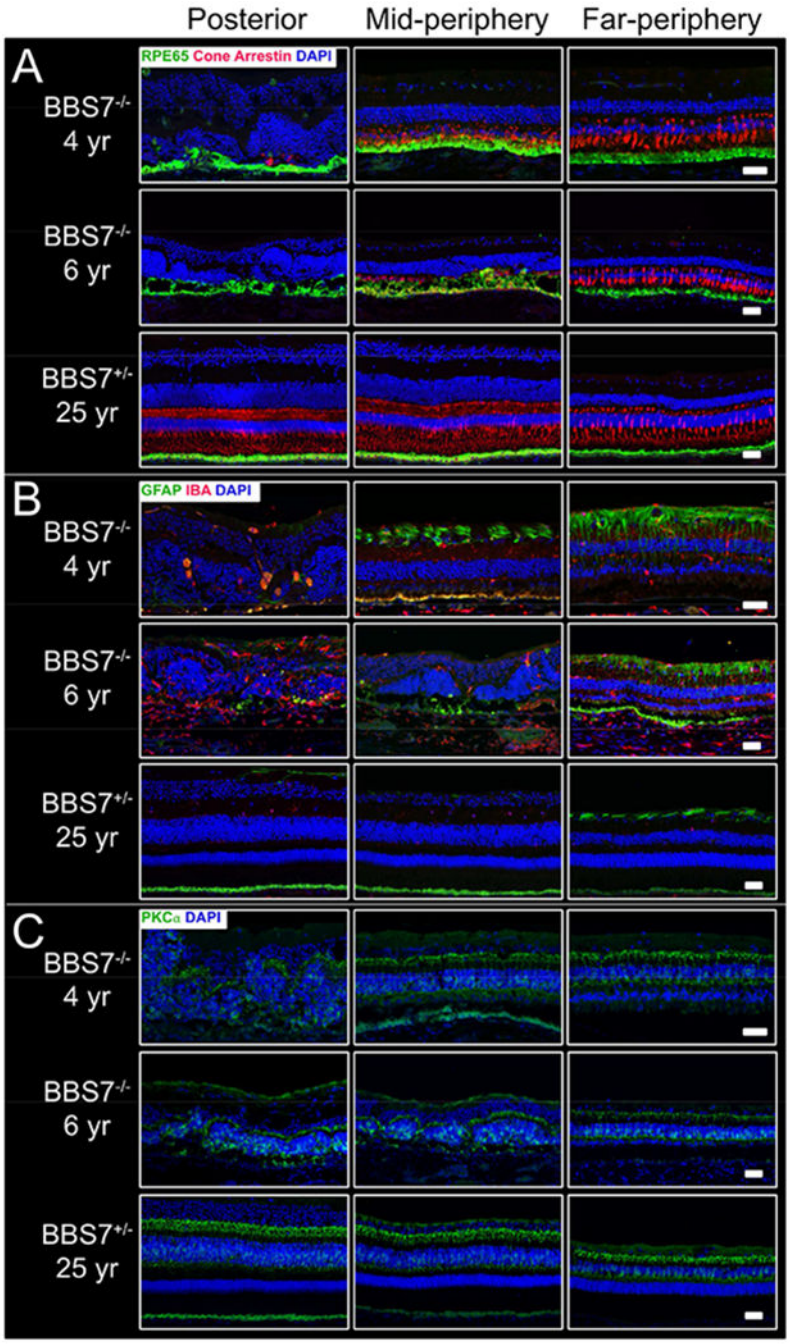

Fig. 6.

Immunohistochemical analysis of retinal disease progression in *BBS7*$^{-/-}$ macaques Case 1 (4 years) and Case 2 (6 years), and in a 25-year-old *BBS7*$^{+/-}$ heterozygote with normal retina shown for comparison. A) Retinal pigment epithelium (RPE65 antibody) and cone cells (cone arrestin). B) Müller glia (GFAP) and reactive microglial cells (IBA1). C) Rod bipolar cells (PKCα). For all panels, DAPI indicates nuclear stain. In both cases, posterior retina was significantly more affected with severe atrophy throughout all cell layers. With increasing eccentricity from the macula, the retina appeared more organized with proper

lamination, presence of cone photoreceptors, and rod bipolar cells with normal positioning of dendrites and axon terminal boutons. The greatest difference between the two cases was observed in the severity of mid-peripheral retinal degeneration, which was worse in the older animal. White scale bars represent 50 μm.

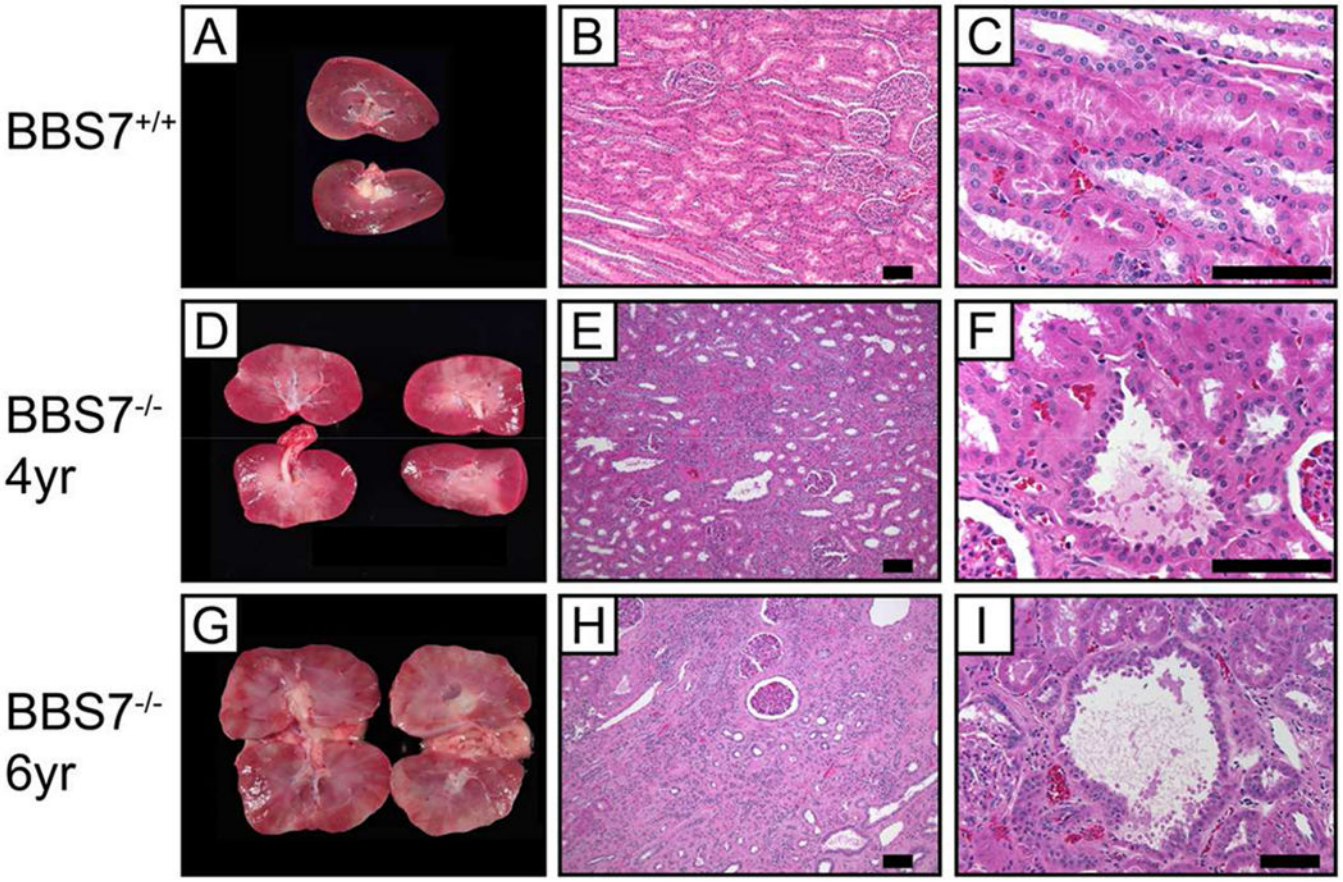

Fig. 7.

Renal pathology in *BBS7*−/− macaques Case 1 (4 years) and Case 2 (6 years). Compared with a normal control (A), kidneys of *BBS7*−/− macaques (D,G) were scarred with extensive parenchymal loss grossly. H&E stained sections of affected macaques (E,F,H,I) demonstrated loss of nephrons with replacement fibrosis, tubule atrophy and ectasia. Cystic tubules were lined with attenuated to hyperplastic epithelium (F,I) which occasionally formed micropapillary projections (I). These microscopic findings were not present in the normal control (B,C). Black scale bars represent 100 μm.

Table 1.

Demographics and organ phenotypes for *BBS*$^{-/-}$ rhesus monkeys

Case	1	2	3	Heterozygotes
Sex	M	F	F	
Age (years)	4	6	3.5 - 4 *	
Body wt (kg)	3.7	6.6	7.3	
Retinal imaging In vivo	NA	Macular atrophy, vessel loss, severe thinning with loss of distinct layers, most severe centrally; diffuse high FAF with macular low FAF	Macular atrophy, thinned vessels, severe thinning with loss of distinct layers, most severe centrally; diffuse high FAF with macular low FAF	Normal (16-year-old male, 25-year-old male)
Retinal histopathology	Loss of photoreceptors, abnormal RPE, severe thinning, disorganized inner retina, abundant microglia and gliosis; most severe centrally	Loss of photoreceptors and RPE, severe thinning, disorganized inner retina, abundant microglia and gliosis; most severe centrally; more advanced than Case 1	NA (living case)	Normal (25-year-old male)
Kidney pathology	*Histopathology:* Interstitial fibrosis, dilated tubules, hyperplastic epithelium	*Abdominal ultrasound:* Deranged cortical architecture. *Histopathology:* Medullary cyst, severe cortical loss, nephron loss, fibrosis, cystic and atrophic tubules	*Abdominal ultrasound:* Diffusely increased echogenicity (nonspecific indicator of renal disease)	*Abdominal ultrasound and histopathology:* Renal cyst in 25-year-old male; normal structure in 10 other heterozygotes
Brain Wt (g)	82.9 vs 96.1±8.7 g for normal males **	75.5 vs 86.1α8.0 g for normal females **	NA	94.9±8.2 g for males (n=6) 83.6±4.9 g for females (n=6)
Brain volume by MRI (ml)	NA	NA	74.1 vs 105.6±10.1 for age-matched controls (n=18)	NA
Other Brain MRI findings	NA	NA	Enlarged right lateral ventricle	NA
Behavior	“Stargazing”, vision deficits; otherwise normal	Vision deficits; otherwise normal	Vision deficits; otherwise normal	No abnormalities noted
Gonads	Testes small and histologically immature	Normal ovaries by histopathology	Small uterus by ultrasound	No abnormalities noted; normal fertility

* Period of observation reported here.

** Normative data from Herndon et al., 1998

NA: Data not available.

Table 2.

List of antibodies, sources, and dilutions

Antibodies	Source	Dilution
PKC-α	Santa Cruz Biotechnology (H-7) sc-8378	1:500
PKC-α	Sigma P4334 RRID:AB_477345	1:40,000
RPE65	Abcam ab13826	1:500
IBA	Wako Chemicals 019-19741	1:500
GFAP	UC Davis/NIH NeuroMab Facility 73-240 (clone N206A/8)	1:100
Cone arrestin	Gift from Dr. Cheryl Craft, University of Southern California	1:20,000